

An Integrative Multi-omics Analysis based on Liquid-liquid Phase Separation Delineates Distinct Subtypes of Lower-grade Glioma and Identifies a Prognostic Signature

Jianglin Zheng

Wuhan Xiehe Hospital: Wuhan Union Hospital

Zhipeng Wu

Wuhan Xiehe Hospital: Wuhan Union Hospital

Yue Qiu

Wuhan Xiehe Hospital: Wuhan Union Hospital

Xuan Wang

Wuhan Xiehe Hospital: Wuhan Union Hospital

Xiaobing Jiang (✉ 2004xh0835@hust.edu.cn)

Wuhan Xiehe Hospital: Wuhan Union Hospital <https://orcid.org/0000-0001-8844-0286>

Primary research

Keywords: liquid-liquid phase separation, lower-grade glioma, genomic alterations, tumor immune microenvironment, immunotherapy

Posted Date: October 12th, 2021

DOI: <https://doi.org/10.21203/rs.3.rs-870729/v1>

License:  This work is licensed under a Creative Commons Attribution 4.0 International License.

[Read Full License](#)

Abstract

Background: Emerging evidences have indicated that the aberrant liquid-liquid phase separation (LLPS) leads to the dysfunction of biomolecular condensates, thereby contributing to the tumorigenesis and progression. Nevertheless, it remains unclear whether or how the LLPS of specific molecules affects the prognosis and tumor immune microenvironment (TIME) of patients with lower-grade glioma (LGG).

Methods: We integrated the transcriptome information of 3585 LLPS-related genes to comprehensively evaluate the LLPS patterns of 423 patients with LGG in The Cancer Genome Atlas (TCGA) cohort. Then, we systematically demonstrated the differences among four LLPS subtypes based on multi-omics analyses. In addition, we constructed the LLPS-related prognostic risk score (LPRS) for individualized integrative assessment.

Results: Based on the expression profiles of 85 scaffolds, 355 regulators, and 3145 clients in LGG, we identified four LLPS subtypes, namely LS1, LS2, LS3 and LS4.

We confirmed that there were significant differences in prognosis, clinicopathological features, cancer hallmarks, genomic alterations, TIME patterns and immunotherapeutic responses among four LLPS subtypes. In addition, a prognostic signature called LPRS was constructed for individualized integrative assessment. LPRS exhibited a robust predictive capacity for prognosis of LGG patients in multiple cohorts. Moreover, LPRS was found to be correlated with clinicopathological features, cancer hallmarks, genomic alterations and TIME patterns of LGG patients. The predictive power of LPRS in response to immune checkpoint inhibitor (ICI) therapy was also prominent.

Conclusions: This study provided a novel classification of LGG patients based on LLPS. The constructed LPRS might facilitate individualized prognosis prediction and better immunotherapy options for LGG patients.

Introduction

Currently, the understanding of the pathogenesis of human tumors is incomplete, which dramatically limits the development of effective treatment strategies. Classic perspective is that hallmark characteristics of tumors are acquired through gene-level alterations that disrupt the 'lock-and-key' binding type between crucial proteins. However, emerging evidences indicate that a large proportion of tumor malignant phenotypes originate from the intrinsically disordered domains (IDRs) of protein or RNA molecules [1–3]. Notably, many of these IDRs are regulated by the liquid-liquid phase separation (LLPS) process [4–6]. LLPS refers to separating a homogeneous liquid phase containing macromolecular components into two different phases, one accumulates specific macromolecules forming biomolecular condensates, including stress granule, processing body (P-body) and nuclear speckle, and so on, another in which the identical macromolecules are depleted [7]. LLPS is a dynamic process involving the scaffolds, regulators and clients. Scaffolds appear to be essential for the structural integrity of biomolecular condensates. Regulators ensure that biomolecular condensates function properly. Clients

reside in condensates only under certain conditions, and often contain components that specifically bind to components in the scaffolds [8]. Accumulating studies have revealed that the LLPS process is nonnegligible for the development and treatment of human diseases, including tumors [9, 10]. For instance, the deubiquitylase USP42 leads to nuclear speckle mRNA splicing through dynamic LLPS process to promote tumorigenesis [11]. The LLPS of YAP promoted by interferon- γ induces cancer resistance to anti-PD-1 immunotherapy [12]. Hence, we consider that exploring the role of LLPS should be a fruitful area in oncology research, and will further benefit the understanding of tumor pathogenesis, the prediction of prognosis, and the individualized selection of treatment options.

Diffuse lower-grade glioma (LGG) is the most common primary central nervous system tumor, characterized by high recurrence and progression rates even with the continuing development of multiple treatment modalities [13]. The marked heterogeneities in prognosis and therapeutic response of patients are always major clinical challenges. In the above context, this study attempted to identify and quantify such heterogeneities based on the LLPS patterns of LGG patients. Finally, four LLPS subtypes of LGG patients in The Cancer Genome Atlas (TCGA) cohort were identified with distinct prognosis, clinicopathological features, hallmark characteristics, genomic alterations, tumor immune microenvironment (TIME) patterns and immunotherapeutic responses. The constructed prognostic signature, namely LLPS-related prognostic risk score (LPRS), exhibited robust predictive power in the prognosis and the response to immune checkpoint inhibitor (ICI) therapy. Our findings might facilitate individualized prognosis prediction and better immunotherapy options for LGG patients.

Methods

Patient population and data resource of LLPS

The RNA sequencing (RNA-seq) data and clinical information of LGG patients were extracted from TCGA (<https://portal.gdc.cancer.gov/>), the Chinese Glioma Genome Atlas (CGGA; <http://www.cgga.org.cn/>) and Rembrandt (<http://gliovis.bioinfo.cnio.es/>) databases. Patients with missing survival data or overall survival (OS) < 30 days, or without clear histopathological diagnosis were excluded from further analyses. In total, five cohorts were gathered, including TCGA, CGGA-mRNAseq_693, CGGA-mRNAseq_325, CGGA-mRNA-arry_301 and Rembrandt cohorts. The TCGA cohort served as a training cohort and others were used as validation cohorts. We also downloaded the RNA-seq data of 1152 normal brain tissues from the Genotype-Tissue Expression (GTEx; <https://gtexportal.org/home/>) database. All RNA-seq data were obtained in the format of fragments per kilobase of exon model per million mapped reads (FPKM) normalized. The clinicopathological features of LGG patients in five cohorts were summarized in Table 1.

Table 1

Demographics and clinicopathological features of LGG patients in the training and validation cohorts.

| | Training cohort | Validation cohorts | | | |
|--|-------------------|--------------------|-------------------|--------------------|-----------|
| | TCGA | CGGA-mRNAseq_693 | CGGA-mRNAseq_325 | CGGA-Mrna-arry_301 | Rembrandt |
| No. of samples | 423 | 420 | 170 | 158 | 119 |
| Age (mean \pm SD; years) | 43.28 \pm 13.34 | 40.32 \pm 10.36 | 40.39 \pm 10.85 | 39.58 \pm 10.57 | NA |
| Gender | | | | | |
| Male | 234 | 235 | 105 | 90 | 59 |
| Female | 189 | 185 | 65 | 68 | 37 |
| NA | 0 | 0 | 0 | 0 | 23 |
| Survival status | | | | | |
| Alive | 317 | 223 | 82 | 85 | 34 |
| Dead | 106 | 197 | 88 | 73 | 85 |
| Pretreatment KPS | | | | | |
| <80 | 33 | NA | NA | NA | NA |
| \geq 80 | 224 | NA | NA | NA | NA |
| NA | 166 | NA | NA | NA | NA |
| Histology | | | | | |
| Astrocytoma | 154 | 254 | 110 | 102 | 80 |
| Oligodendroglioma | 110 | 137 | 60 | 38 | 34 |
| Oligoastrocytoma | 159 | 29 | 0 | 18 | 0 |
| NA | 0 | 0 | 0 | 0 | 5 |
| WHO grade | | | | | |
| II | 201 | 172 | 97 | 105 | 63 |
| Continued | | | | | |
| III | 222 | 248 | 73 | 53 | 56 |
| IDH status | | | | | |
| Mutant | 344 | 288 | 125 | 104 | NA |
| Wild type | 77 | 94 | 44 | 1 | NA |
| NA | 2 | 38 | 1 | 53 | NA |

| 1p19q status | | | | | |
|-----------------------------|-----|-----|-----|-----|----|
| Codeletion | 141 | 125 | 55 | 16 | 8 |
| Non-codeletion | 282 | 257 | 113 | 33 | 13 |
| NA | 0 | 38 | 2 | 109 | 98 |
| MGMT promoter status | | | | | |
| Methylated | 351 | 200 | 84 | 43 | NA |
| Unmethylated | 72 | 129 | 70 | 106 | NA |
| NA | 0 | 91 | 16 | 9 | NA |
| TERT status | | | | | |
| Mutant | 120 | NA | NA | NA | NA |
| Wild type | 140 | NA | NA | NA | NA |
| NA | 163 | NA | NA | NA | NA |

The data resource of LLPS (DrLLPS; <http://llps.biocuckoo.cn/>) is an integrative database for proteins involved in LLPS, which has incorporated 150 scaffolds that are drivers of LLPS, 987 regulators that contribute in modulating LLPS, and 8148 clients, all of which were experimentally identified in multiple eukaryotic species [14]. Our study subjects were homo sapiens. Finally, a total of 85 scaffolds, 355 regulators and 3145 clients with available gene-expression data were screened out for subsequent analyses.

Identification of LLPS subtypes of LGG patients

The expression data of these LLPS-related genes was normalized with $\log_2(\text{FPKM}+1)$ transformation for the differential expression analysis between LGG tissues and normal brain tissues. Then, the differentially expressed genes (DEGs; $P < 0.05$, $|\log_2\text{FC}| > 1.5$) were retained for univariate Cox regression analyses to identify the prognostic LLPS-related DEGs. The Gene Ontology (GO) and Kyoto Encyclopedia of Genes and Genomes (KEGG) pathway analyses were conducted for the functional annotation via the “clusterProfiler” package of R. Based on the expression profiles of prognostic LLPS-related DEGs. The non-negative matrix factorization (NMF) consensus clustering was performed through the R package “NMF” to obtain LLPS subtypes of LGG patients. The cophenetic, dispersion and silhouette indicators were used to determine the optimal clustering number. We applied the t-distributed stochastic neighbor embedding (tSNE) algorithm to confirm the reliability of clustering results. The Kaplan-Meier (K-M) survival curves were used to determine the survival difference among different LLPS subtypes. On the basis of 50 hallmark gene sets retrieved from Molecular Signatures Database (MSigDB), the enrichment

levels of 50 hallmarks of different LLPS subtypes were quantified by single-sample Gene Set Enrichment Analysis (ssGSEA).

Analyses of genomic alterations

The somatic mutation profiles sorted in the form of mutation annotation format (MAF) were obtained from TCGA database. By using the R package “Maftools”, we analyzed and visualized the mutation profiles and frequencies of genes in different LLPS subtypes. The tumor mutation burden (TMB) was calculated as mutations per megabase (mut/Mb) [15]. Also, the copy number alteration (CNA) data of LGG patients were acquired from TCGA database. We used GISTIC2.0 to identify significant amplifications or deletions in the whole genome [16]. The CNA burden was defined as the total number of genes with copy number changes at the focal and arm levels [17].

Assessment of TIME and immunotherapeutic responses

ESTIMATE algorithm was employed to calculate the immune scores, stromal scores, ESTIMATE scores and tumor purity of LGG patients via the R package “estimate” [18]. The enrichment scores of 29 immune signatures were quantified by ssGSEA [19]. Based on the ssGSEA Z-scores of those 29 immune signatures, patients were classified into high-/low- immunity subtypes. We also applied the CIBERSORT algorithm with 1,000 permutations to calculate the compositions of 22 types of immune cells [20]. The Tumor Immune Dysfunction and Exclusion (TIDE) algorithm was performed online (<http://tide.dfci.harvard.edu/>) to assess the potential response to ICI therapy. Patients with lower TIDE scores or higher microsatellite instability (MSI) scores were more likely to show stronger responses to ICI therapy. Another method, unsupervised subclass mapping (<https://cloud.genepattern.org/gp>), was also utilized to predict the response to ICI therapy based on the gene-expression similarity between LGG patients and melanoma patients treated with anti-PD1 and anti-CTLA4 therapy [21, 22].

Construction and validation of a LLPS-related signature

To identify the hub genes related to LLPS subtypes, the weighted gene co-expression network analysis (WGCNA) was performed on the expression profiles of prognostic LLPS-related DEGs by using the R package “WGCNA” [23, 24]. The optimal soft-thresholding power was selected according to the standard scale-free model fitting index R². Then, we calculated the module eigengenes to investigate the correlations between the modules and LLPS subtypes. The hub genes in the modules most closely correlated to LLPS subtypes were identified. Interactions among these hub genes were visualized by using the STRING database (<https://www.string-db.org/>). To construct a LLPS-related prognostic signature, the hub genes were included into the least absolute shrinkage and selection operator (LASSO) Cox regression. Finally, the LPRS was calculated as follows:

$$\text{LPRS} = \sum_{i=1}^n \text{Coef}_i * x_i$$

where x_i and Coef_i refer to the expression level of selected hub genes and corresponding LASSO coefficient, respectively. The prognostic value of the LPRS was evaluated by K–M survival curves with log-rank tests in both training and validation cohorts. The receiver operating characteristic (ROC) curve analyses were applied to assess the accuracy of LPRS in predicting OS of LGG patients. The independent prognostic value of LPRS was determined by univariate and multivariate Cox regression analyses. Moreover, we utilized the random-effects meta-analysis model to calculate the pooled hazard ratio (HR) of LPRS.

The role of LPRS in two independent ICI therapy cohorts

To verify the role of LPRS in predicting the response to ICI therapy, two independent ICI therapy cohorts with available genomic and clinical information were included in our study: advanced urothelial cancer treated with atezolizumab, an anti-PD-L1 antibody (IMvigor210 cohort) [25], and metastatic melanoma with treatment of pembrolizumab, an anti-PD-1 antibody (GSE78220 cohort) [26]. We transformed the gene expression profiles into the TPM format for a higher comparability. The LPRS of each patient was calculated to evaluate its association with the response to ICI therapy.

Statistical analysis

PERL programming language (version 5.32.0) was used to preprocess the RNA-seq data. R software (version 4.0.2) were applied for all statistical analyses and graph visualizations. The Chi-square test was executed for the comparison of categorical variables between groups. Statistical significance for continuous variables between two groups or more than two groups was estimated by Student t test or the Kruskal–Wallis test, respectively. The correlation between two parameters was assessed through the Spearman correlation analysis. Two-tailed $P < 0.05$ was considered statistically significant.

Results

LLPS-related genes

The overall flow diagram of this study was presented in Fig. 1. The detailed information of 3585 LLPS-related genes in homo sapiens was obtained from the DrLLPS, of which 85 were scaffolds (2.37%), 355 were regulators (9.9%) and 3145 were clients (87.73%; Additional file 1: Fig. S1A and Additional file 7: Table S1). Then, the transcriptome data of these 3585 LLPS-related genes were obtained from TCGA cohort and the GTEx database. The heatmap showed an obvious distinction in the expression of LLPS-related genes between LGG samples and normal samples (Additional file 1: Fig. S1B). Further differential

expression analysis identified 443 LLPS-related DEGs, of which 170 were upregulated and 273 were downregulated in LGG samples compared with normal samples (Fig. 2A and Additional file 8: Table S2). By intersecting these DEGs with the prognostic LLPS-related genes obtained through univariate Cox regression analysis (Additional file 9: Table S3), 225 prognostic LLPS-related DEGs were identified (Fig. 2B), of which 3 were scaffolds, 24 were regulators and 198 were clients (Additional file 1: Fig. S1C). The top 10 significantly enriched GO terms and KEGG pathways for these prognostic LLPS-related DEGs were shown in Fig. S1D and E (see Additional file 1).

Identification of LLPS subtypes in TCGA cohort

Based on the expression profiles of 225 prognostic LLPS-related DEGs, we performed NMF to identify LLPS subtypes in TCGA cohort. We selected 4 as the optimal clustering number, which was decided by the cophenetic, dispersion and silhouette indicators (Additional file 2: Fig. S2). Then, a total of 423 LGG patients were categorized into four subtypes (Fig. 2C), namely LS1 (n=73), LS2 (n=78), LS3 (n=227) and LS4 (n=45). The tSNE showed robust differences in distribution among four LLPS subtypes (Fig. 2D). The prominent differences in the expression of 225 prognostic LLPS-related DEGs were also observed in the heatmap (Fig. 2E). The K-M survival curve revealed that there was distinct survival difference among four LLPS subtypes (Fig. 2F). LS1 had the worst survival outcome, whereas LS3 had the best survival outcome.

Subsequently, we compared the demographics and clinicopathological features of LGG patients in four LLPS subtypes. As illustrated in Fig. 3A, LS1 had more patients with age greater than or equal to 45 years compared with other subtypes. There were no significant differences among subtypes regarding gender distribution. The proportion of patients with Karnofsky Performance Score (KPS) greater than or equal to 80 was higher in LS3 than other subtypes. A higher percentage of deaths was observed in LS1 and LS4. Astrocytoma was more common in LS1, but oligodendroglioma was more common in other three subtypes. LS1 and LS4 had a significantly higher proportion of World Health Organization (WHO) grade III glioma compared with LS2 and LS3. There were also significant differences in molecular pathology among four LLPS subtypes. LGG patients with IDH wild type, or 1p19q non-codeletion, or MGMT promoter (MGMTp) unmethylated, or TERT mutant were more frequent in LS1.

To explore the underlying molecular mechanism related to the LLPS subtypes of LGG, we performed ssGSEA based on the transcriptome data of 50 gene sets retrieved from MSigDB. The ssGSEA Z-score was applied to quantify the levels of 50 hallmarks, and was visually illustrated by the heatmap (Fig. 3B). Compared with LS2 and LS3, LS1 and LS4 was more correlated with the hallmarks related to cell cycle and DNA repair, especially LS4, which may suggest an active proliferation of cancer cells. In addition, LS1 was positively associated with many cancer-related hallmarks, including glycolysis, epithelial mesenchymal transition (EMT), angiogenesis, hypoxia, apoptosis, inflammation and immunity. For further validation, we screened out a total of 507 upregulated genes ($\log_2FC > 1$ and $P < 0.05$) in LS1, and 121 upregulated genes ($\log_2FC > 1$ and $P < 0.05$) in LS4 (Fig. 3C, D), which were subsequently submitted to

GO enrichment analyses. The enriched biological processes of upregulated genes in LS1 and LS4 were consistent with the results of ssGSEA (Fig. 3E, F). The above results might explain the poor survival of LS1 and LS4 to some extent.

Comprehensive analyses of genomic alterations among LLPS subtypes

To gain a further insight into the disparity in the genomic layer, we compared the somatic mutation profiles and CNA landscapes among LLPS subtypes. First, LS1 and LS4 had significantly higher TMB and mutation counts than LS2 and LS3 (Fig. 4A). The somatic mutation profiles revealed that LS1 possessed specific top mutated genes compared with other three LLPS subtypes (Fig. 4B). EGFR was the most commonly mutated gene in LS1, followed by PTEN, whereas IDH1 and TP3 were the most two frequently mutated genes in LS2, LS3 and LS4. Next, we also noticed that there were clear differences in the degree of CNA burden among LLPS subtypes (Fig. 4C). It showed a trend that compared with LS2 and LS3, LS1 and LS4 had relatively higher burdens of gain and loss at both focal and arm levels. The distribution of Gistic score across all autosomes in LLPS subtypes was visualized in Fig. 4D. The results described above demonstrated an active genomic alteration in LS1 and LS4, which was likely due to their stronger proliferation ability of cancer cells.

TIME and immunotherapeutic responses in different LLPS subtypes

Growing studies have begun to characterize the potential role of LLPS in regulating TIME and sensitivity to immunotherapy [12, 27]. Hence, we tried to compare the TIME patterns and immunotherapeutic responses among different LLPS subtypes. The ESTIMATE algorithm was firstly performed to quantify the constituents of the TIME of LGG. The results revealed that LS1 had highest immune, stromal, and ESTIMATE scores, and lowest tumor purity compared with other three subtypes. An opposite trend was observed in LS2 and LS4 (Fig. 5A). Then, LGG patients were classified into high-/low- immunity subtypes based on the ssGSEA Z-scores of 29 immune signatures. LS1 consisted of more proportions of high-immunity subtype, whereas LS2, LS3 and LS4 contained mainly low-immunity subtype ($P < 0.001$; Fig. 5B). The distribution of ssGSEA Z-score of 29 immune signatures was presented in Fig. 5C and D. There were significant differences in immune cell infiltrations and immune functions among four LLPS subtypes. Most notably, LS1 showed higher infiltration of most immune cells, and more robust immune functions than other three subtypes. Another algorithm, CIBERSORT, was also utilized to described the proportion of 22 immune cells in different LLPS subtypes, which was displayed in Fig. 5E.

We then compared the expression levels of immune checkpoints among LLPS subtypes. Compared with other subtypes, LS1 had significantly higher expression levels of all ten immune checkpoints, including PD-1 and its ligands (PD-L1 and PD-L2), CTLA-4 and its ligands (CD80 and CD86), LAG-3, TIM-3, IDO1

and B7H3 (Fig. 5F). Currently, ICI therapy has undoubtedly been a very promising strategy of immunotherapy, which caused a major breakthrough in antitumor treatment. Thus, we further used the TIDE algorithm to predict the response to ICI therapy of different LLPS subtypes. Our results revealed that the TIDE score was significantly decreased in LS1 and LS4 (Fig. 5G). The proportions of responders in LS1 and LS4 were nearly twofold that in LS2 and LS3 subtypes ($P < 0.001$; Fig. 5H). We also observed that compared with LS2 and LS3, LS1 and LS4 had higher MSI scores, which has been considered to be an indicator of effective immunotherapy (Fig. 5I). Moreover, we performed subclass mapping analysis to predict the response to ICI therapy, including PD-1 and CTLA-4 inhibitors, of the four LLPS subtypes. LS1 was found to be more sensitive to PD-1 inhibitor (Bonferroni corrected $P = 0.001$), while LS2 showed no response to CTLA-4 inhibitor (Bonferroni corrected $P = 0.044$; Fig. 5J). All these findings suggested that the LLPS patterns of LGG might play a crucial role in regulating the TIME patterns and immunotherapeutic responses.

Construction and validation of a prognostic signature based on LLPS-related hub genes

To identify the LLPS-related hub genes, WGCNA analysis was performed with the transcriptome data of 225 prognostic LLPS-related DEGs. We selected 2 as the optimal soft-thresholding power based on the standard scale-free model fitting index R^2 (Additional file 3: Fig. S3A). Then, a total of 10 gene modules were obtained. Based on the previous findings, there were similarities in terms of survival, genomic alteration and immune characteristic between LS1 and LS4, also between LS2 and LS3. Thus, LS1 and LS4, and LS2 and LS3, were merged together, respectively. Among these 10 models, the brown module containing 26 genes exhibited the highest correlation with LS1 and LS4, and the green module containing 17 genes showed the highest correlation with LS2 and LS3 (Fig. 6A, B). Then, the genes in these two models were deemed as LLPS-related hub genes, and were picked for subsequent analyses. Fig. S3B and C (see Additional file 3) showed the top 10 enriched GO terms and KEGG pathways for the genes of the green and brown modules. As shown in the interaction networks, there were 15 genes and 11 edges in the green module, and 22 genes and 92 edges in the brown module with a threshold weight > 0.15 (Additional file 3: Fig. S3D, E).

Next, these forty-three LLPS-related hub genes were incorporated into the LASSO Cox regression in the TCGA cohort, twelve of which stood out for the construction of a LLPS-related prognostic signature (Additional file 3: Fig. S3F and Fig. 6C). Fig. 6D exhibited the LASSO coefficients of each selected gene in this signature. There were nine protective genes and three risky genes for survival outcomes. The K-M survival curves of these 12 selected genes were shown in Fig. S4 (see Additional file 4). Then, the LPRS of each LGG patient was calculated by summing the product of the expression levels of each selected LLPS-related hub gene and corresponding LASSO coefficients. The median LPRS was used to stratify patients into high-LPRS and low-LPRS subgroups. As shown in the K-M survival curves, high-LPRS patients exhibited worse OS in TCGA cohort (Fig. 6E). Consistent results were obtained in four independent validation cohorts (Fig. 6F-I). Additionally, the high accuracy of LPRS in predicting 1-, 3- and 5-year OS

was confirmed by the ROC curves (Additional file 5: Fig. S5A). According to the univariate and multivariate Cox regression analyses, LPRS was an independent prognostic indicator for OS in all cohorts (Additional file 5: Fig. S5B). Further, meta-analysis was performed, and revealed that the overall pooled HR of LPRS was 1.91 (95% CI = 1.39-2.63; Fig. 6J).

Correlation of LPRS with clinicopathological features, genomic alterations and TIME patterns

The prognostic value of LPRS has been well elucidated. Then, we sought to explore its clinical relevance in TCGA cohort. As shown in Fig. 7A, LPRS was ranked from low to high to show the correlation between LPRS and clinicopathological features. There were significant differences between high- and low-LPRS subgroups in terms of age, survival status, histology, WHO grade, IDH status, 1p19q status, MGMTp status, TERT status, immunity subtypes and LLPS subtypes. The attribute changes of each patient were visualized by an alluvial diagram (Fig. 7B). We also compared the levels of LPRS between subgroups stratified by different clinicopathological features. Patients with the clinicopathological features of age \geq 45 years, death, astrocytoma, WHO grade III, IDH wild type, 1p19q non-codeletion and MGMTp unmethylated presented significantly higher levels of LPRS, whereas no LPRS differences were observed between patients stratified by gender, KPS and TERT status (Additional file 6: Fig. S6A). In addition, we found that the high-immunity subtype was associated with a higher LPRS than low-immunity subtype, and LPRS was ranked in increasing order for LS3, LS2, LS4 and LS1 (Additional file 6: Fig. S6A).

To better characterize the LLPS-related prognostic signature, we tested the correlation between the cancer hallmarks and LPRS. A correlation heatmap revealed that LPRS was significantly positively correlated with many well-known hallmarks of cancer, including DNA repair and cell cycle-related hallmarks (Fig. 7C). As expected, further analyses demonstrated that LPRS was markedly positively linked with TMB, mutation counts, burden of copy number gain and loss at focal-level, and burden of copy number gain at arm-level (Fig. 7D). These data indicated to some extent that a higher LPRS represents a higher frequency of genomic alterations.

Given that LPRS was associated with different immunity subtypes, we took further insight into the detailed differences in TIME patterns as the LPRS changes. The correlation between LPRS and 29 immune signatures was illustrated by a correlation heatmap (Fig. 7E). Then, LPRS was significantly positively correlated with the immune, stromal, and ESTIMATE scores, but negatively correlated with tumor purity, which indicating that the infiltration levels of immune and stromal cells increase with the elevation of LPRS (Fig. 7F). Further correlation analyses were carried out between LPRS and the infiltration levels of 22 immune cells quantified by the CIBERSORT algorithm. It turned out that LPRS was positively correlated with memory resting CD4+ T cells, M1 macrophages and Tregs, and was negatively correlated with activated mast cells and monocytes (Additional file 6: Fig. S6B). In addition, LPRS was observed to be positively correlated with the expression levels of ten immune checkpoints (Additional file 6: Fig. S6C).

The role of LPRS in predicting the response to ICI therapy

ICI therapy represented by PD-1, PD-L1 and CTLA-4 inhibitors has undoubtedly achieved encouraging progress in the therapeutic landscape of cancer. However, the considerable heterogeneity in therapeutic response has long been a major challenge to improve survival outcomes for glioma patients. Hence, we focused on the role of LPRS in predicting the response to ICI therapy. In TCGA cohort, patients with higher LPRS showed lower level of TIDE and higher level of MSI score (Fig. 8A, B). Based on TIDE algorithm, the high-LPRS subgroup contained a higher proportion of responders to ICI therapy compared with low-LPRS subgroup (Fig. 8C). Besides, the LPRS of responders was significantly higher than that of non-responders (Fig. 8D). Above all, we speculated that high-LPRS patients could benefit more from ICI therapy than low-LPRS patients. To make our findings more convincing, we next investigated whether the LPRS could predict patients' response to ICI therapy in two independent ICI therapy cohorts, namely IMvigor210 (anti-PD-L1 cohort) and GSE78220 (anti-PD-1 cohort). In both cohorts, there were significantly higher proportion of complete response (CR) or partial response (PR) in the high-LPRS subgroup (Fig. 8E, F). Patients with the outcome of CR or PR exhibited significantly higher level of LPRS than patients with the outcome of stable disease (SD) or progressive disease (PD) (Fig. 8G, H). An overall satisfactory accuracy of LPRS for predicting the response to ICI therapy was confirmed by the ROC curves (Fig. 8J, K). Altogether, our findings strongly indicated that the LPRS was associated with the response to ICI therapy, and has the potential to serve as a response indicator in clinical practice.

Discussion

Evidence is now mounting that LLPS process plays an integral role in the tumorigenesis and progression [10]. Moreover, the formation of different TIME patterns has also been shown to be correlated with LLPS due to its involvement in the regulation of immune signaling [27, 28]. Therefore, we supposed that a comprehensive exploration of LLPS-related biomarkers held great promise for the identification of novel subtypes of tumors, and the prediction of prognosis and immunotherapeutic response. In this study, we exclusively focused on LGG patients. Based on the expression profiles of 225 prognostic LLPS-related DEGs, we identified four LLPS subtypes of 423 LGG patients by using NMF algorithm. Then, significant differences among four LLPS subtypes were observed regarding prognosis, clinicopathological features, cancer hallmarks, genomic alterations, TIME patterns and immunotherapeutic responses. To make individualized integrative assessments, a prognostic signature, namely LPRS, was constructed via the WGCNA algorithm and LASSO Cox regression. Results revealed that LPRS was correlated with prognosis, clinicopathological features, genomic alterations and TIME patterns of LGG patients. The predictive power of LPRS in response to ICI therapy was also prominent.

Representative hallmarks of tumors include sustained proliferation, angiogenesis, EMT and genome rearrangements, and so on. How do tumors acquire these hallmark characteristics? In recent years, the field of LLPS is changing the way researchers and clinicians are now thinking about the acquisition of malignant characteristics of tumors [10]. For instance, MYC has the potential to form phase-separated transcription condensates by binding to super-enhancers, which can lead to the expression of VEGF and

promote angiogenesis [29]. The LLPS of transcriptional coactivators, YAP and TAZ, is involved in the activation of EMT [30–32]. The abnormal LLPS of ENL is enriched in genomic loci of chromosomes, and recruits large numbers of related transcription complexes, resulting in genome rearrangements in cancer [33, 34]. In this study, different LLPS subtypes of LGG patients exhibited distinct tumor hallmarks characteristics quantized by ssGSEA. The LS1 subtype was characterized by glycolysis, angiogenesis, EMT, hypoxia-responsive activation and regulation of apoptotic signaling pathway. However, the critical tumor hallmarks of LS4 were related to cell cycle and genome stability, which corresponded with the active genomic alteration of LS4. Compared with LS2 and LS3, LS1 and LS4 showed significant malignant progression features, which provided a possible explanation for the worse prognosis of LS1 and LS4. Simultaneously, the constructed LPRS also showed a significant correlation with these well-known hallmarks of tumors. These results provided compelling support for the nonnegligible role of LLPS in conferring specific hallmarks of tumors.

The classical view held that tumors could be divided into three different TIME patterns: immune-inflamed, immune-excluded, and immune-desert. It has long been known that glioma is dominated by immune-excluded and immune-desert patterns, which contribute, to a large extent, to the immune escape of glioma cells and the immunotherapy resistance of patients. The formation of specific TIME pattern is an immensely complex process involving numerous factors. Recent reports about the role of LLPS in innate and adaptive immunity shed new light on this field. For example, the LLPS of cyclic GMP-AMP synthase (cGAS) promotes the secondary messenger cyclic GMP-AMP (cGAMP) production and innate immune signaling [35]. A large proportion of biomolecules in the transmembrane signaling receptors of T cells might phase separate into clusters to facilitate the transduction of signals and regulate immune responses of tumors [36]. In this study, LS1 had higher immune scores and stroma scores, but lower tumor purity compared with other subtypes, indicating that LS1 was surrounded by more nontumor components. Furthermore, LS1 displayed the activation of adaptive immune pathway and the infiltration of tumor infiltrating lymphocyte infiltration. Thus, it can be considered that LS1 corresponded to the immune-inflamed pattern, and was likely to respond well to immunotherapy. Subsequent prediction of the response to ICI therapy confirmed this speculation. Based on the TIDE algorithm, LS1 presented relatively lower TIDE score and higher MSI score compared with LS2 and LS3. In addition, subclass mapping analysis revealed that LS1 responded remarkably well to PD-1 inhibitor. Taking together, these findings strongly suggested that the established LLPS subtypes would contribute to the differential recognition of TIME patterns, and help to identify patients suitable for ICI therapy. Follow-up studies are warranted to determine the detailed mechanism of how LLPS processes regulate the specific formation of TIME patterns.

Given the multifaceted heterogeneities among four LLPS subtypes, we considered that it was feasible to construct a prognostic signature for the quantification of such heterogeneities, and also for the individualized integrative assessments. As expected, the constructed LPRS not only exhibited a close correlation with clinicopathological features, representative cancer hallmarks, genomic alterations and TIME patterns of LGG patients, but also possessed a prominent power in predicting prognosis and response to ICI therapy. LPRS was composed of twelve selected LLPS-related genes, of which two were

regulators and ten were clients. The regulator TNPO1, also known as Karyopherin- β 2, has been reported to inhibit the LLPS of an RNA-binding protein Fused in Sarcoma (FUS) and escort it into the nucleus [37]. Another regulator, SFRP2, is required for P-body assembly [19]. Of these ten clients, CADPS, CRTAC1, SCD5 and TPM1 can form postsynaptic density [38]. FAM204A and PPIF are involved in nucleolus [39–41]. SMU1 participates in the formation of stress granule [42]. Other three clients can form variety types of biomolecular condensates (FAM110B: centrosome, spindle pole body; TOP2A: nucleolus, centrosome, spindle pole body and P-body; XRN2: nucleolus, P-body and stress granule) [41, 43–51]. As is already evident, what we currently know about these LLPS-related genes is almost exclusively confined to the forming types of biomolecular condensates that they are involved in. Thus, a more in-depth mechanism of how the LLPS processes that underlie the assembly of various biomolecular condensates affect the occurrence and development of tumors needs to be investigated in the future.

Nonetheless, several limitations of this study should be addressed. First, all analyses were performed based on the retrospective data of public databases, using the prospective multi-center cohorts will produce more reliable results. Second, due to the limitation of immunotherapy cohorts with publicly available transcriptional data and clinical information, we could only assess the predictive power of LPRS in response to ICI therapy by using the cohorts of urothelial cancer and metastatic melanoma. Finally, bioinformatic analyses are not able to deeply elucidate the molecular mechanisms, experimental evidences are indispensable to further exploration.

Conclusion

Taken together, we divided LGG patients into four LLPS subtypes with distinct prognosis, clinicopathological features, cancer hallmarks, genomic alterations, TIME patterns and immunotherapeutic responses. In addition, a prognostic signature, LPRS, was proposed for individualized integrative assessment. The findings might facilitate individualized prognosis prediction and better immunotherapy options for LGG patients, and further studies are needed to clarify this point.

Abbreviations

IDRs: intrinsically disordered domains; LLPS: liquid-liquid phase separation; P-body: processing body; LGG: lower-grade glioma; TCGA: The Cancer Genome Atlas; TIME: tumor immune microenvironment; LPRS: LLPS-related prognostic risk score; ICI: immune checkpoint inhibitor; RNA-seq: RNA sequencing; CGGA: Chinese Glioma Genome Atlas; OS: overall survival; GTEx: Genotype-Tissue Expression; FPKM: fragments per kilobase of exon model per million mapped reads; DrLLPS: data resource of LLPS; DEGs: differentially expressed genes; GO: Gene Ontology; KEGG: Kyoto Encyclopedia of Genes and Genomes; NMF: non-negative matrix factorization; tSNE: t-distributed stochastic neighbor embedding; K-M: Kaplan-Meier; MSigDB: Molecular Signatures Database; ssGSEA: single sample gene set enrichment analysis; MAF: Mutation annotation format; TMB: tumor mutation burden; CNA: copy number alteration; TIDE: Tumor Immune Dysfunction and Exclusion; MSI: microsatellite instability; WGCNA: weighted gene co-expression network analysis; LASSO: least absolute shrinkage and selection operator; ROC: receiver

operating characteristic; HR: hazard ratio; KPS: Karnofsky Performance Score; WHO: World Health Organization; MGMTp: MGMT promoter; EMT: epithelial mesenchymal transition; CR: complete response; PR: partial response; SD: stable disease; PD: progressive disease; cGAS: cyclic GMP-AMP synthase; cGAMP: cyclic GMP-AMP; FUS: Fused in Sarcoma

Declarations

Ethics approval and consent to participate

Not applicable.

Consent for publication

Not applicable.

Availability of data and materials

Publicly available datasets were analyzed in this study. This data can be found here: the data analyzed in this study can be acquired in the DrLLPS, (<http://llps.biocuckoo.cn/>), TCGA (<https://portal.gdc.cancer.gov/>), CGGA (<http://www.cgga.org.cn/>), Rembrandt (<http://gliovis.bioinfo.cnio.es/>) and GTEx (<https://gtexportal.org/home/>) websites.

Competing interests

The authors declare no competing interests.

Funding

This work was supported by National Natural Science Foundation of China (No.81974390).

Authors' contributions

Jianglin Zheng and Zhipeng Wu conceived and designed this study. Jianglin Zheng, Zhipeng Wu and Yue Qiu performed the data analysis, figures plotting and writing. Xuan Wang and Xiaobing Jiang were responsible for the critical reading of the manuscript. All authors participated in interpreting the results and revision of the manuscript and approved the submitted version.

Acknowledgements

We all authors sincerely acknowledge the contributions from the DrLLPS, TCGA, CGGA, Rembrandt and GTEx projects.

References

1. McSwiggen DT, Mir M, Darzacq X, Tjian R. Evaluating phase separation in live cells: diagnosis, caveats, and functional consequences. *Genes Dev.* 2019;33(23-24):1619–34.
2. Vacic V, Iakoucheva LM. Disease mutations in disordered regions—exception to the rule? *Mol Biosyst.* 2012;8(1):27–32.
3. Aguzzi A, Altmeyer M. Phase Separation: Linking Cellular Compartmentalization to Disease. *Trends in cell biology.* 2016;26(7):547–58.
4. Nott TJ, Petsalaki E, Farber P, Jervis D, Fussner E, Plochowietz A, et al. Phase transition of a disordered nuage protein generates environmentally responsive membraneless organelles. *Molecular cell.* 2015;57(5):936–47.
5. Pak CW, Kosno M, Holehouse AS, Padrick SB, Mittal A, Ali R, et al. Sequence Determinants of Intracellular Phase Separation by Complex Coacervation of a Disordered Protein. *Molecular cell.* 2016;63(1):72–85.
6. Altmeyer M, Neelsen KJ, Teloni F, Pozdnyakova I, Pellegrino S, Grofte M, et al. Liquid demixing of intrinsically disordered proteins is seeded by poly(ADP-ribose). *Nature communications.* 2015;6:8088.
7. Alberti S, Dormann D. Liquid-Liquid Phase Separation in Disease. *Annual review of genetics.* 2019;53:171–94.
8. Banani SF, Rice AM, Peeples WB, Lin Y, Jain S, Parker R, et al. Compositional Control of Phase-Separated Cellular Bodies. *Cell.* 2016;166(3):651–63.
9. Taniue K, Akimitsu N. Aberrant phase separation and cancer. *The FEBS journal* 2021.
10. Cai D, Liu Z, Lippincott-Schwartz J. Biomolecular Condensates and Their Links to Cancer Progression. *Trends Biochem Sci.* 2021;46(7):535–49.
11. Liu S, Wang T, Shi Y, Bai L, Wang S, Guo D, et al: USP42 drives nuclear speckle mRNA splicing via directing dynamic phase separation to promote tumorigenesis. *Cell death and differentiation* 2021.
12. Yu M, Peng Z, Qin M, Liu Y, Wang J, Zhang C, et al. Interferon- γ induces tumor resistance to anti-PD-1 immunotherapy by promoting YAP phase separation. *Molecular cell.* 2021;81(6):1216–30.e1219.
13. Ostrom QT, Cioffi G, Gittleman H, Patil N, Waite K, Kruchko C, et al. CBTRUS Statistical Report: Primary Brain and Other Central Nervous System Tumors Diagnosed in the United States in 2012–2016. *Neuro Oncol.* 2019;21(Suppl 5):v1–100.
14. Ning W, Guo Y, Lin S, Mei B, Wu Y, Jiang P, et al. DrLLPS: a data resource of liquid-liquid phase separation in eukaryotes. *Nucleic Acids Res.* 2020;48(D1):D288–95.
15. Mayakonda A, Lin DC, Assenov Y, Plass C, Koeffler HP. Maftools: efficient and comprehensive analysis of somatic variants in cancer. *Genome research.* 2018;28(11):1747–56.

16. Mermel CH, Schumacher SE, Hill B, Meyerson ML, Beroukhir R, Getz G. GISTIC2.0 facilitates sensitive and confident localization of the targets of focal somatic copy-number alteration in human cancers. *Genome biology*. 2011;12(4):R41.
17. Shen R, Li P, Li B, Zhang B, Feng L, Cheng S. Identification of Distinct Immune Subtypes in Colorectal Cancer Based on the Stromal Compartment. *Frontiers in oncology*. 2019;9:1497.
18. Yoshihara K, Shahmoradgoli M, Martínez E, Vegesna R, Kim H, Torres-Garcia W, et al. Inferring tumour purity and stromal and immune cell admixture from expression data. *Nature communications*. 2013;4:2612.
19. He Y, Jiang Z, Chen C, Wang X. Classification of triple-negative breast cancers based on Immunogenomic profiling. *Journal of experimental clinical cancer research: CR*. 2018;37(1):327.
20. Newman AM, Liu CL, Green MR, Gentles AJ, Feng W, Xu Y, et al. Robust enumeration of cell subsets from tissue expression profiles. *Nature methods*. 2015;12(5):453–7.
21. Hoshida Y, Brunet JP, Tamayo P, Golub TR, Mesirov JP. Subclass mapping: identifying common subtypes in independent disease data sets. *PloS one*. 2007;2(11):e1195.
22. Roh W, Chen PL, Reuben A, Spencer CN, Prieto PA, Miller JP, et al: Integrated molecular analysis of tumor biopsies on sequential CTLA-4 and PD-1 blockade reveals markers of response and resistance. *Science translational medicine* 2017, 9(379).
23. Zhang B, Horvath S. A general framework for weighted gene co-expression network analysis. *Stat Appl Genet Mol Biol*. 2005;4:Article17.
24. Langfelder P, Horvath S. WGCNA: an R package for weighted correlation network analysis. *BMC Bioinform*. 2008;9:559.
25. Mariathasan S, Turley SJ, Nickles D, Castiglioni A, Yuen K, Wang Y, et al. TGF β attenuates tumour response to PD-L1 blockade by contributing to exclusion of T cells. *Nature*. 2018;554(7693):544–8.
26. Hugo W, Zaretsky JM, Sun L, Song C, Moreno BH, Hu-Lieskovan S, et al. Genomic and Transcriptomic Features of Response to Anti-PD-1 Therapy in Metastatic Melanoma. *Cell*. 2016;165(1):35–44.
27. Xia S, Chen Z, Shen C, Fu TM. Higher-order assemblies in immune signaling: supramolecular complexes and phase separation. *Protein & cell*; 2021.
28. Huoh YS, Hur S. Death domain fold proteins in immune signaling and transcriptional regulation. *FEBS J* 2021.
29. Boija A, Klein IA, Sabari BR, Dall'Agnese A, Coffey EL, Zamudio AV, et al. Transcription Factors Activate Genes through the Phase-Separation Capacity of Their Activation Domains. *Cell*. 2018;175(7):1842–55 e1816.
30. Cai D, Feliciano D, Dong P, Flores E, Gruebele M, Porat-Shliom N, et al. Phase separation of YAP reorganizes genome topology for long-term YAP target gene expression. *Nat Cell Biol*. 2019;21(12):1578–89.
31. Franklin JM, Guan KL. YAP/TAZ phase separation for transcription. *Nat Cell Biol*. 2020;22(4):357–8.

32. Lu Y, Wu T, Gutman O, Lu H, Zhou Q, Henis YI, et al. Phase separation of TAZ compartmentalizes the transcription machinery to promote gene expression. *Nat Cell Biol.* 2020;22(4):453–64.
33. Wan L, Chong S, Xuan F, Liang A, Cui X, Gates L, et al. Impaired cell fate through gain-of-function mutations in a chromatin reader. *Nature.* 2020;577(7788):121–6.
34. Gao Y, Li P. Acquired 'Phase Separation' Underlies Aberrant Cell Fate Control? *Trends Biochem Sci.* 2020;45(6):457–8.
35. Du M, Chen ZJ. DNA-induced liquid phase condensation of cGAS activates innate immune signaling. *Science.* 2018;361(6403):704–9.
36. Ahluwalia P, Ahluwalia M, Mondal AK, Sahajpal N, Kota V, Rojiani MV, et al: Immunogenomic Gene Signature of Cell-Death Associated Genes with Prognostic Implications in Lung Cancer. *Cancers* 2021, 13(1).
37. Yoshizawa T, Ali R, Jiou J, Fung HYJ, Burke KA, Kim SJ, et al. Nuclear Import Receptor Inhibits Phase Separation of FUS through Binding to Multiple Sites. *Cell.* 2018;173(3):693–705 e622.
38. Bayés A, Collins MO, Croning MD, van de Lagemaat LN, Choudhary JS, Grant SG. Comparative study of human and mouse postsynaptic proteomes finds high compositional conservation and abundance differences for key synaptic proteins. *PloS one.* 2012;7(10):e46683.
39. Fong KW, Li Y, Wang W, Ma W, Li K, Qi RZ, et al. Whole-genome screening identifies proteins localized to distinct nuclear bodies. *J Cell Biol.* 2013;203(1):149–64.
40. Palm D, Simm S, Darm K, Weis BL, Ruprecht M, Schleiff E, et al. Proteome distribution between nucleoplasm and nucleolus and its relation to ribosome biogenesis in *Arabidopsis thaliana*. *RNA Biol.* 2016;13(4):441–54.
41. Andersen JS, Lam YW, Leung AK, Ong SE, Lyon CE, Lamond AI, et al. Nucleolar proteome dynamics. *Nature.* 2005;433(7021):77–83.
42. Jain S, Wheeler JR, Walters RW, Agrawal A, Barsic A, Parker R. ATPase-Modulated Stress Granules Contain a Diverse Proteome and Substructure. *Cell.* 2016;164(3):487–98.
43. Hauge H, Patzke S, Aasheim HC. Characterization of the FAM110 gene family. *Genomics.* 2007;90(1):14–27.
44. Barthelmes HU, Grue P, Feineis S, Straub T, Boege F. Active DNA topoisomerase IIalpha is a component of the salt-stable centrosome core. *J Biol Chem.* 2000;275(49):38823–30.
45. Tavormina PA, Côme MG, Hudson JR, Mo YY, Beck WT, Gorbsky GJ. Rapid exchange of mammalian topoisomerase II alpha at kinetochores and chromosome arms in mitosis. *J Cell Biol.* 2002;158(1):23–9.
46. Maiato H, Sunkel CE. Kinetochores-microtubule interactions during cell division. *Chromosome research: an international journal on the molecular supramolecular evolutionary aspects of chromosome biology.* 2004;12(6):585–97.
47. Hubstenberger A, Courel M, Bénard M, Souquere S, Ernoult-Lange M, Chouaib R, et al. P-Body Purification Reveals the Condensation of Repressed mRNA Regulons. *Molecular cell.*

2017;68(1):144–57.e145.

48. Boisvert FM, Lam YW, Lamont D, Lamond AI. A quantitative proteomics analysis of subcellular proteome localization and changes induced by DNA damage. *Molecular cellular proteomics: MCP*. 2010;9(3):457–70.
49. Scherl A, Couté Y, Déon C, Callé A, Kindbeiter K, Sanchez JC, et al. Functional proteomic analysis of human nucleolus. *Molecular biology of the cell*. 2002;13(11):4100–9.
50. Chahar HS, Chen S, Manjunath N. P-body components LSM1, GW182, DDX3, DDX6 and XRN1 are recruited to WNV replication sites and positively regulate viral replication. *Virology*. 2013;436(1):1–7.
51. Markmiller S, Soltanieh S, Server KL, Mak R, Jin W, Fang MY, et al. Context-Dependent and Disease-Specific Diversity in Protein Interactions within Stress Granules. *Cell*. 2018;172(3):590–604.e513.

Figures

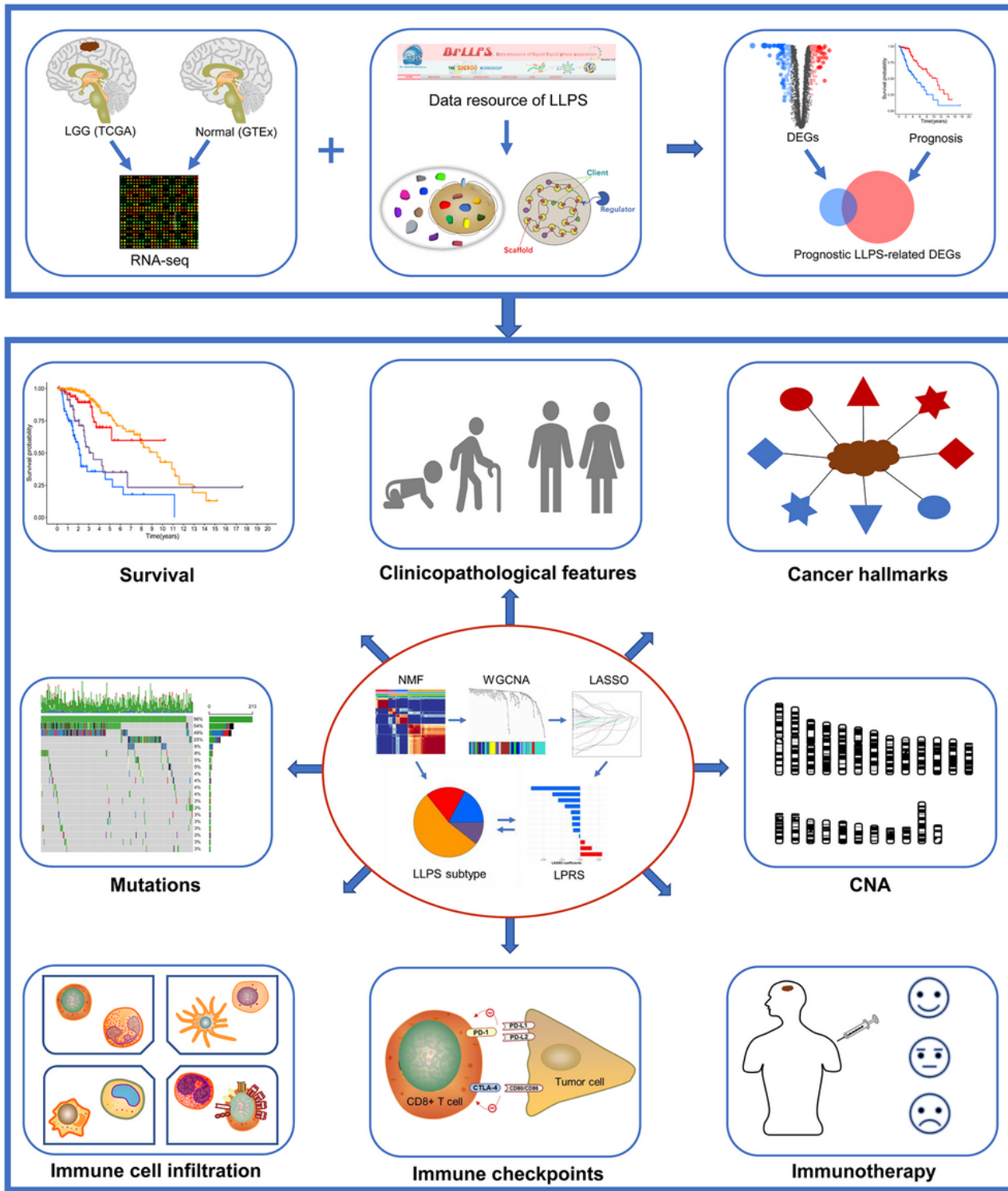


Figure 1

The overall flow diagram of this study.

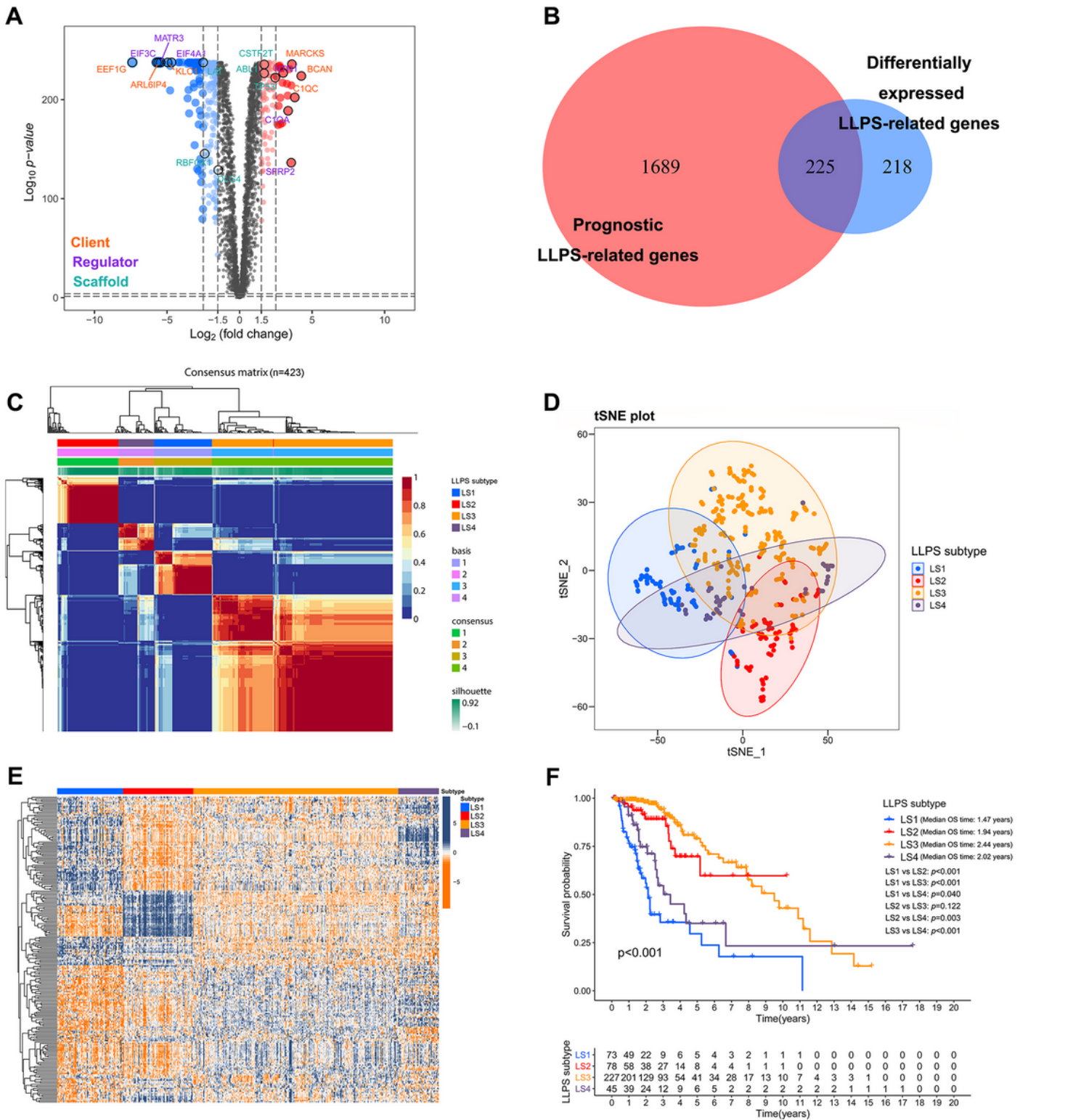


Figure 2

Identification of LLPS subtypes of LGG by using NMF algorithm. A Volcano plot showed DEGs ($P < 0.05$ and $|\log_2FC| > 1.5$) between LGG tissues in TCGA cohort and normal brain tissues in GTEx database. The gene names with top three \log_2FC and lower three \log_2FC were highlighted in the groups of clients, regulators and scaffolds respectively. B Venn diagram identified 225 prognostic LLPS-related DEGs. C Consensus map of NMF clustering. D tSNE plot for the expression profiles of 225 prognostic LLPS-related

DEGs to distinguish LLPS subtypes. E Heatmap showed the expression levels of 225 prognostic LLPS-related DEGs among LLPS subtypes. F Kaplan–Meier survival analysis exhibited significantly different OS among LLPS subtypes.

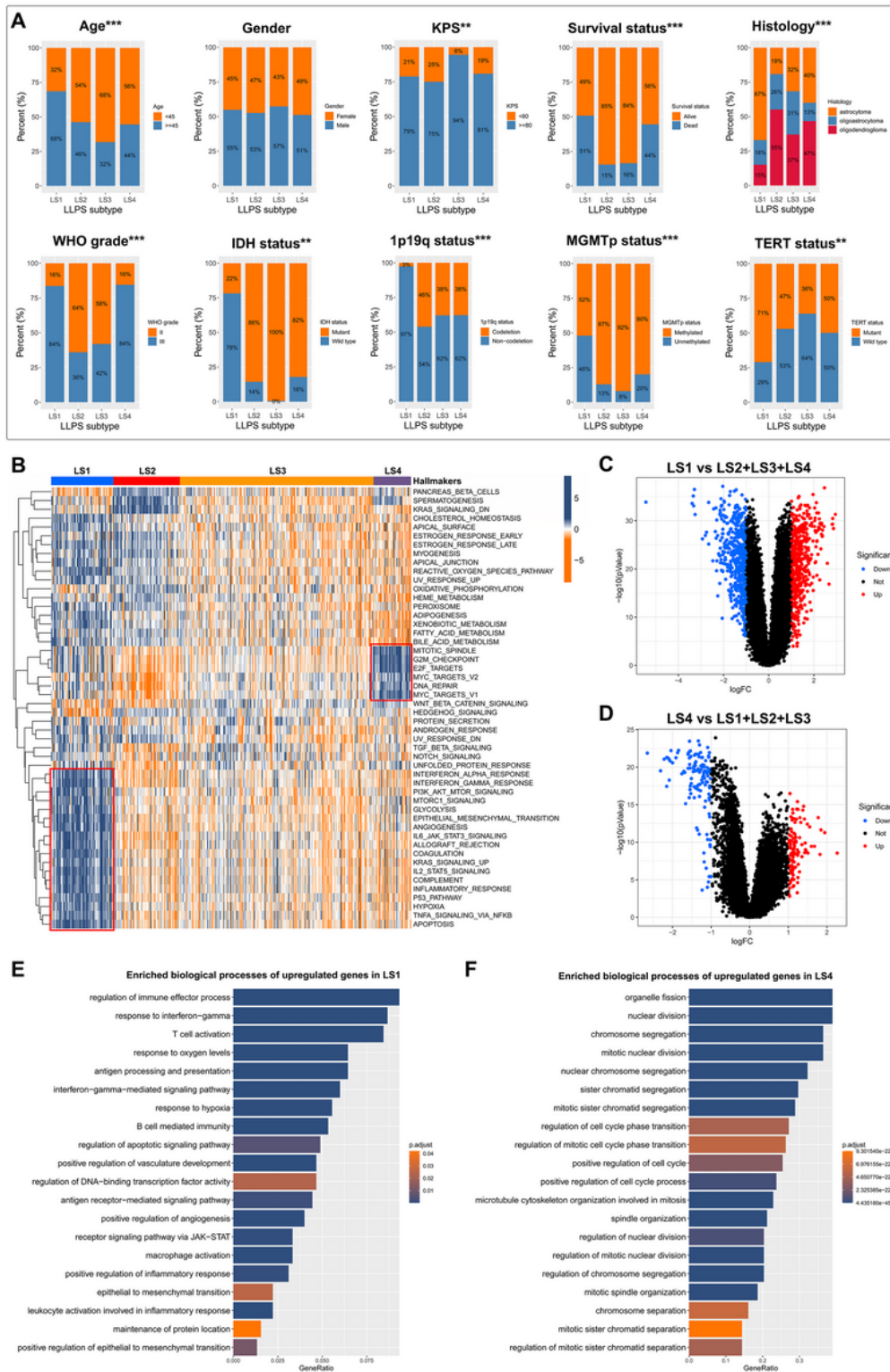


Figure 3

The comparisons of demographics, clinicopathological features and cancer hallmarks among LLPS subtypes. A Comparisons of age, gender, KPS, survival status, histology, WHO grade, IDH status, MGMTp

status and TERT status among LLPS subtypes. B Heatmap illustrated the ssGSEA Z-scores of 50 hallmarks among LLPS subtypes. Blue represented high scores, and yellow represented low scores. The obvious differences were highlighted by red box. C-D Volcano plots showed DEGs ($P < 0.05$ and $|\log_2FC| > 1.5$) in LS1 and LS4 subgroups. E-F Gene Ontology enrichment analysis for significantly upregulated genes in LS1 and LS4, respectively. ** $P < 0.01$, *** $P < 0.001$.

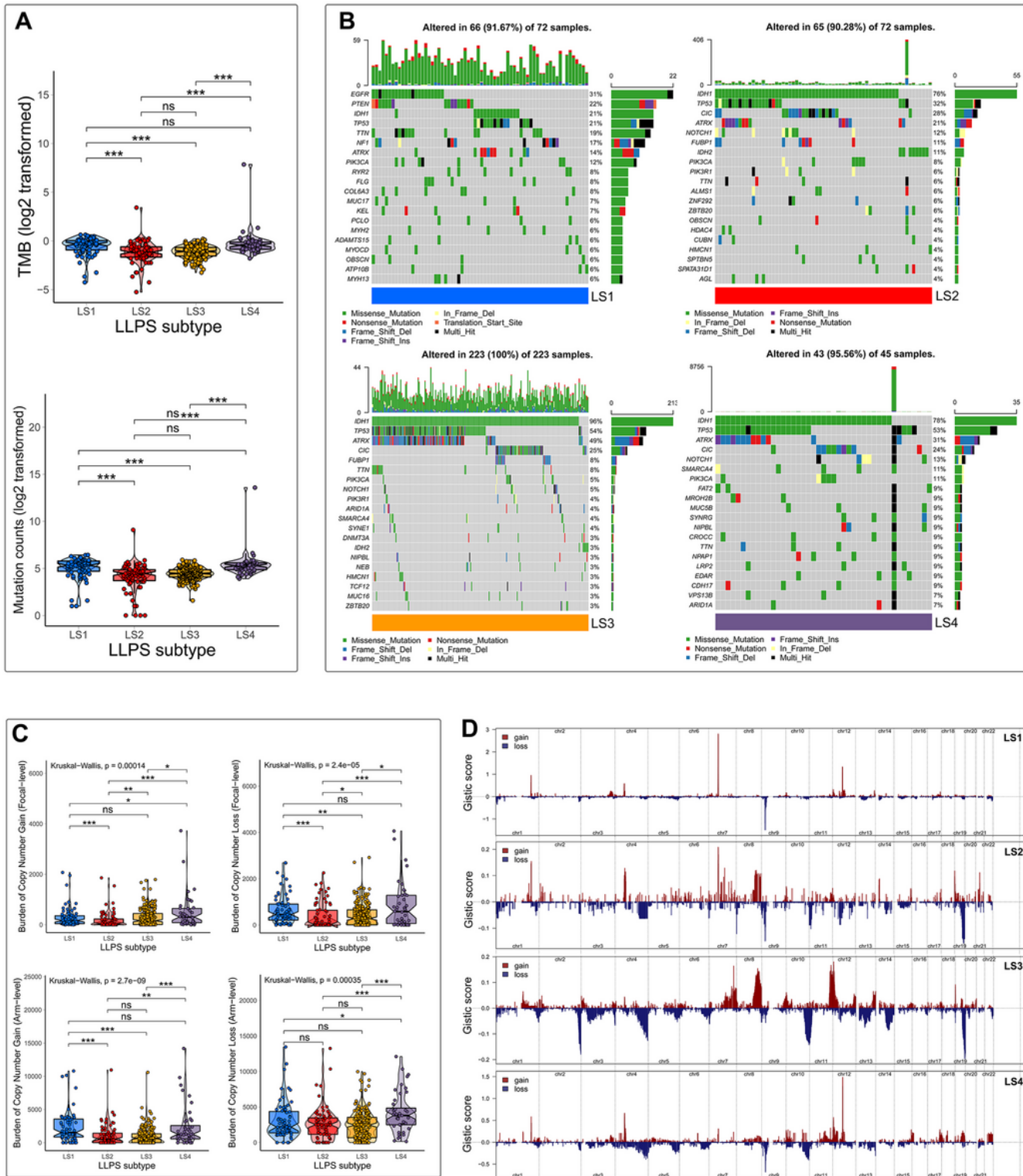


Figure 4

Comprehensive analyses of genomic alterations among LLPS subtypes. A Comparisons of TMB and mutation counts among LLPS subtypes. B Mutation profiles of LLPS subtypes. C Comparisons of CNA burdens at focal and arm levels among LLPS subtypes. D Copy number profiles for LLPS subtypes showed gains and losses of copy numbers of genes, which were placed based on their location on chromosomes, ranging from chromosome 1 to chromosome 22. * $P < 0.05$, ** $P < 0.01$, *** $P < 0.001$, and ns No significance.

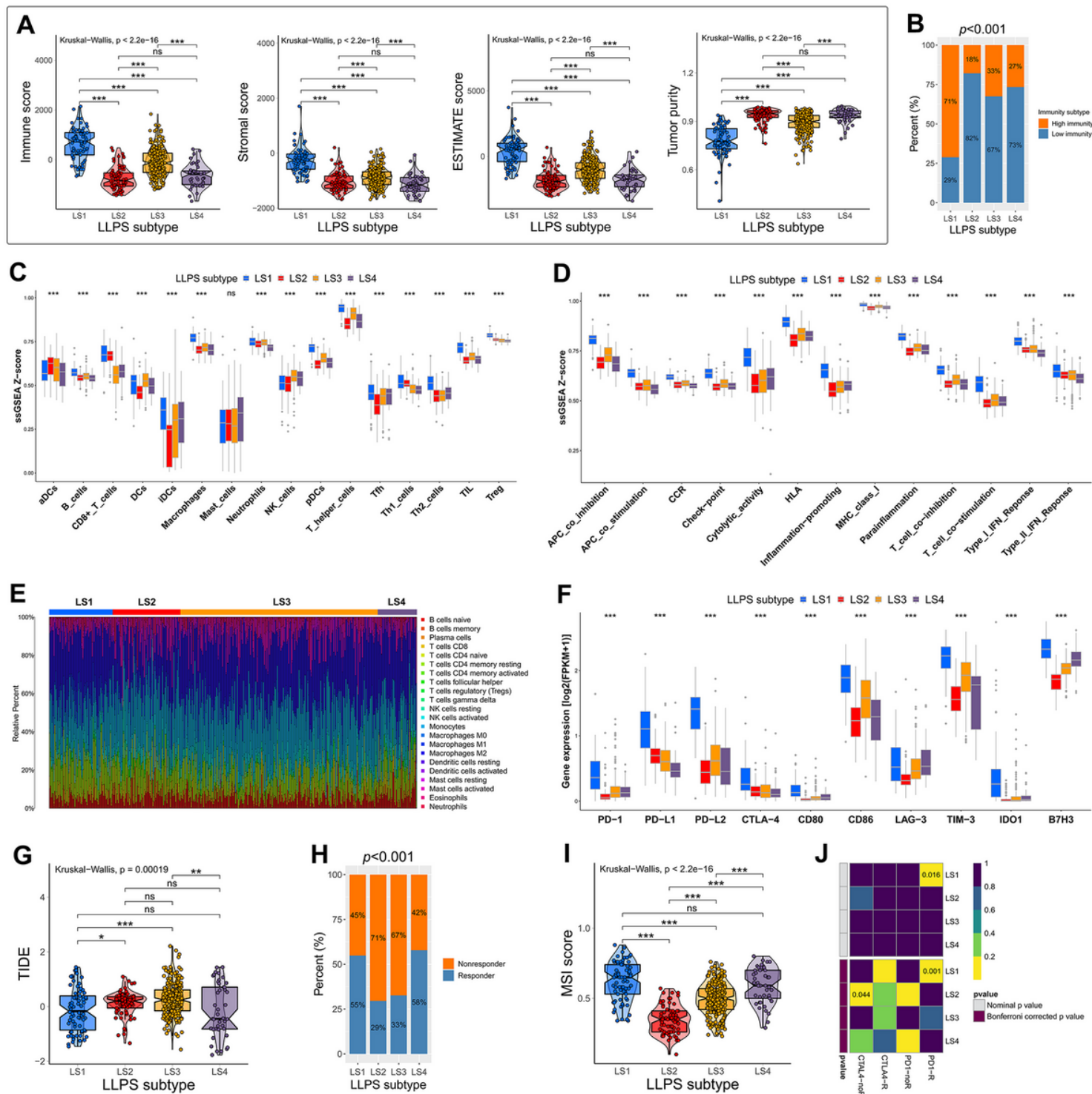


Figure 5

Different TIME patterns and immunotherapeutic responses of LLPS subtypes. A Comparison of immune scores, stromal scores, ESTIMATE scores and tumor purity among LLPS subtypes. B Different proportion of high and low immunity tumors among LLPS subtypes. C-D The levels of immune cell infiltrations and immune functions quantified by ssGSEA Z-score among LLPS subtypes. E The proportion of 22 immune cells quantified by CIBERSORT algorithm among LLPS subtypes. F Comparison of immune checkpoint expressions among LLPS subtypes. G Comparison of TIDE scores among LLPS subtypes. H The proportion of ICI therapy responders predicted by TIDE algorithm among LLPS subtypes. I Comparison of MSI scores among LLPS subtypes. J Subclass mapping analysis for predicting the likelihood of response to ICI therapy of LLPS subtypes. * $P < 0.05$, ** $P < 0.01$, *** $P < 0.001$, and ns No significance.

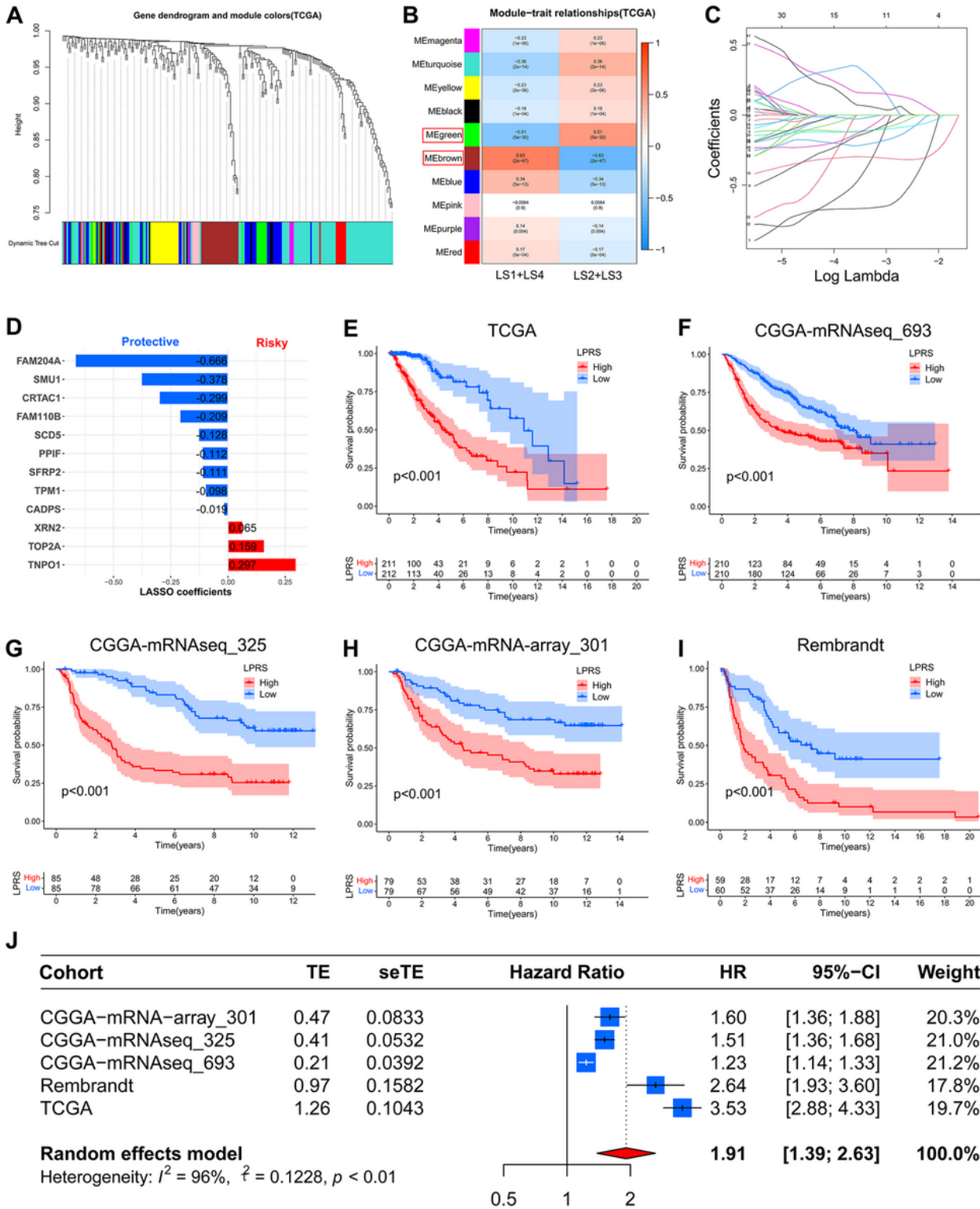


Figure 6

Construction and validation of a LLPS-related prognostic signature for LGG patients. A Gene dendrogram and module colors. B Correlations of 10 modules with LLPS subtypes. The green model and brown model were selected and highlighted with red box. C LASSO regression analysis with minimal lambda value. D LASSO coefficients of selected LLPS-related genes. E-I The Kaplan-Meier survival curves of LPRS in

TCGA, CGGA-mRNAseq_693, CGGA-mRNAseq_325, CGGA-mRNA-arry_301 and Rembrandt cohorts. J Meta-analysis with random-effects showed a pooled hazard ratio (HR) of LPRS.

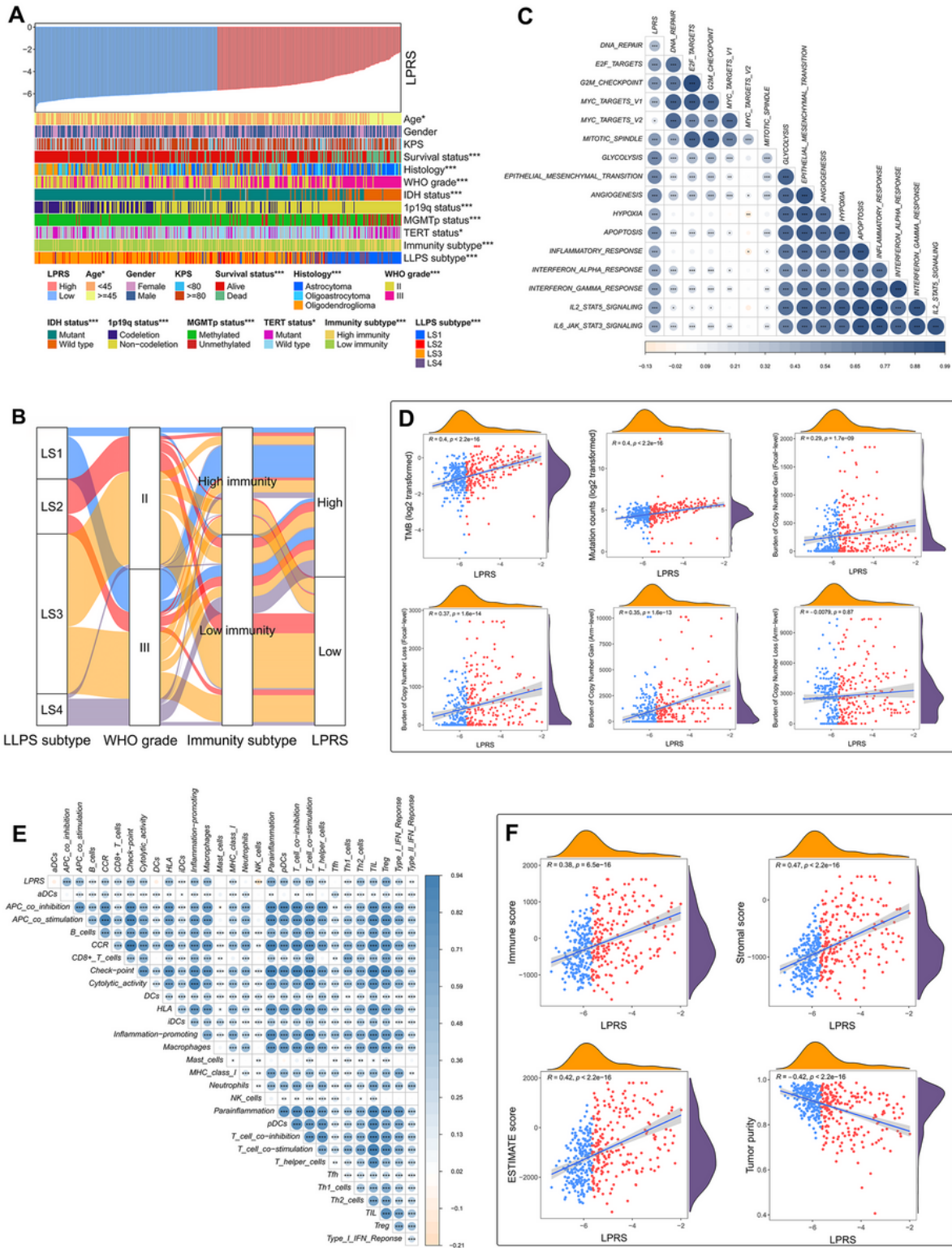


Figure 7

Correlation of LPRS with clinicopathological features, genomic alterations and TIME patterns in TCGA cohort. A An overview of the correspondence between LPRS and other features of LGG patients. B Alluvial diagram showed the attribute changes of LLPS subtypes, WHO grade, immunity subtypes and LPRS. C

Correlation between LPRS and the known cancer hallmarks. D Correlation of LPRS with TMB, mutation counts, and copy number burdens at focal and arm levels. E Correlation between LPRS and the ssGSEA Z-scores of 29 immune signatures. F Correlation of LPRS with immune scores, stromal scores, ESTIMATE scores and tumor purity. * $P < 0.05$, ** $P < 0.01$ and *** $P < 0.001$.

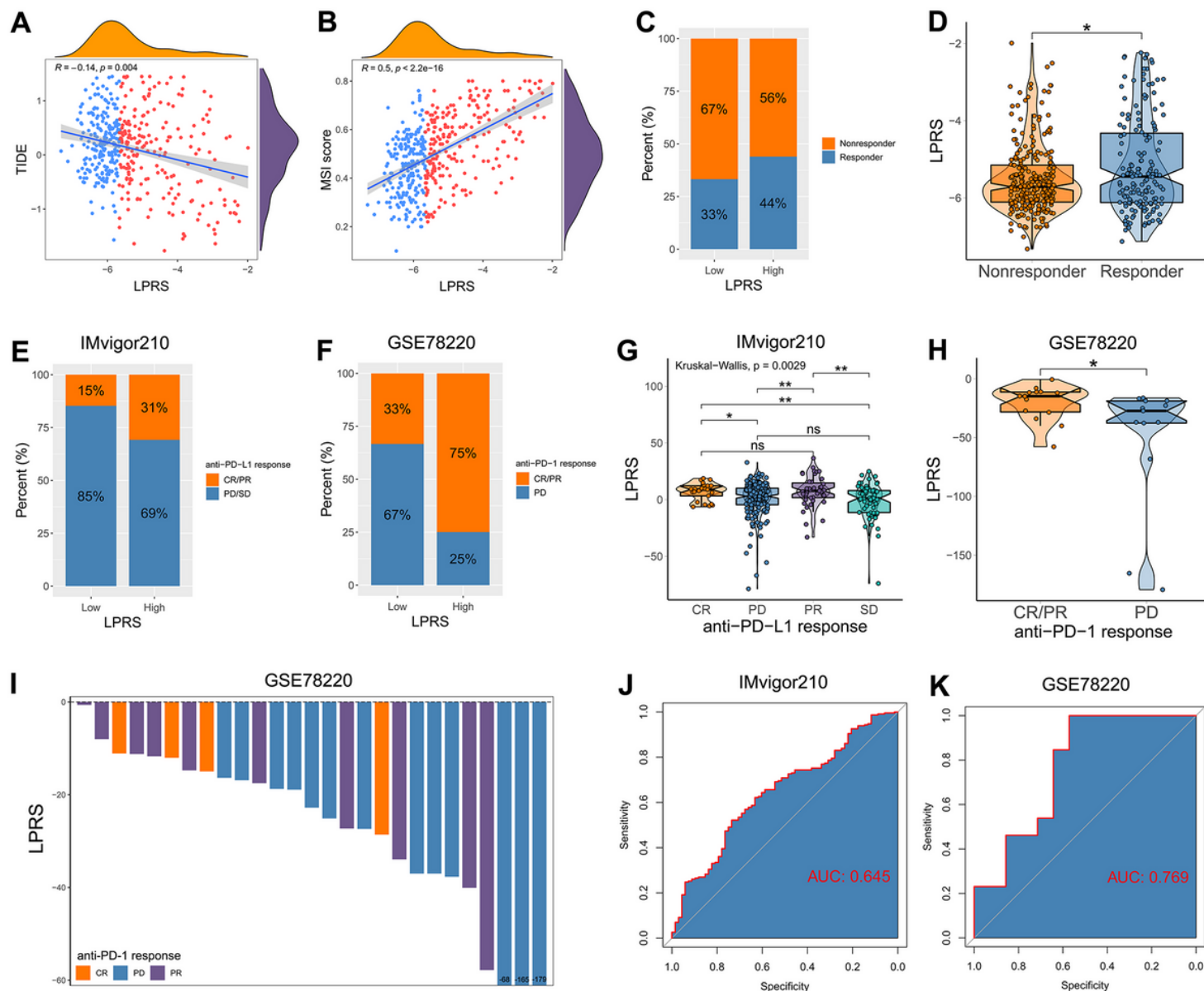


Figure 8

The role of LPRS in predicting the response to ICI therapy. A-B LPRS was correlated with TIDE score and MSI score in TCGA cohort. C The proportion of ICI therapy responders predicted by TIDE algorithm between high-LPRS and low-LPRS subgroups in TCGA cohort. D Comparison of LPRS levels between responders and non-responders in TCGA cohort. E The proportion of patients with response to anti-PD-L1 immunotherapy in IMvigor210 cohort (CR/PR vs. PD/SD: 31% vs. 69% in high-LPRS subgroup, CR/PR vs. PD/SD: 15% vs. 85% in low-LPRS subgroup; $P = 0.001$). F The proportion of patients with response to anti-PD-1 immunotherapy in GSE78220 cohort (CR/PR vs. PD/SD: 75% vs. 25% in high-LPRS subgroup, CR/PR vs. PD/SD: 33% vs. 67% in low-LPRS subgroup; $P = 0.031$). G Comparison of LPRS levels among

the subgroups of different response to anti-PD-L1 immunotherapy in IMvigor210 cohort. H-I Comparison of LPRS levels among the subgroups of different response to anti-PD-1 immunotherapy in GSE78220 cohort. J-K The predictive power of LPRS in patients with anti-PD-L1/ anti-PD-1 immunotherapy (IMvigor210 cohort: AUC = 0.645; GSE78220 cohort: AUC = 0.769). CR, complete response; PR, partial response; PD, progressive disease; SD, stable disease. * P < 0.05, ** P < 0.01, and ns No significance.

Supplementary Files

This is a list of supplementary files associated with this preprint. Click to download.

- [SupplementaryFigureS1.tif](#)
- [SupplementaryFigureS2.tif](#)
- [SupplementaryFigureS3.tif](#)
- [SupplementaryFigureS4.tif](#)
- [SupplementaryFigureS5.tif](#)
- [SupplementaryFigureS6.tif](#)
- [TableS1.xlsx](#)
- [TableS2.xlsx](#)
- [TableS3.xlsx](#)